J Clust Sci (2009) 20:291–305
DOI 10.1007/s10876-008-0229-y

ORIGINAL PAPER

Synthesis and Characterization of Rare Earth Orthovanadate (RVO_4; R = La, Ce, Nd, Sm, Eu & Gd) Nanorods/Nanocrystals/Nanospindles by a Facile Sonochemical Method and Their Catalytic Properties

R. Kalai Selvan · A. Gedanken · P. Anilkumar · G. Manikandan · C. Karunakaran

Received: 24 October 2008 / Published online: 16 December 2008

Abstract We report herein on an efficient sonochemical method for the synthesis of rare earth orthovanadate nanorods/nanoparticles/nanospindles, (general formula RVO_4; R = La, Ce, Nd, Sm, Eu and Gd). TGA, XRD, FTIR, Raman, UV–Vis, and TEM studies are employed for their characterization and for understanding their morphologies. In order to vary the textural properties of the rare earth vanadates, two surfactants, polyethylene glycol (PEG) and amphiphilic triblock copolymer Pluronic P123, are chosen in the preparation. While the sonochemical synthesis in the presence of PEG results in the formation of nearly spherical nanoparticles of $LaVO_4$, $CeVO_4$, $SmVO_4$ and $EuVO_4$, the same technique yields nanorods and nanospindles of $NdVO_4$ and $GdVO_4$, respectively. When P123 is used as the surfactant, the morphologies of RVO_4 are strikingly different, and in most cases nanorods and nanospindles are formed. The photocatalytic activities of the rare earth orthovanadate have been evaluated by studying the degradation of methylene blue, and $CeVO_4$ seems to be the best catalyst in the heterogeneous photolysis. The electrocatalytic activity of the vanadates has been examined by studying the hydrogen evolution reaction using a linear sweep voltammogram technique in 1 M of a H_2SO_4 solution. $GdVO_4$ seems to be the best electrocatalyst.

Keywords Rare earth vanadates · Sonochemical synthesis · Electrocatalyst · Nanorods · Nanoparticles

Electronic supplementary material The online version of this article (doi:10.1007/s10876-008-0229-y) contains supplementary material, which is available to authorized users.

R. Kalai Selvan · A. Gedanken (✉)
Department of Chemistry and Kanbar Laboratory for Nanomaterials, Center for Advanced Materials and Nanotechnology, Bar-Ilan University, Ramat-Gan 52900, Israel
e-mail: gedanken@mail.biu.ac.il

P. Anilkumar · G. Manikandan · C. Karunakaran
Department of Chemistry, Annamalai University, Annamalai Nagar 608 002, India

Introduction

Nanomaterials have gained enormous interest in recent years due to their unique structural, electronic, optical, and magnetic properties, which are often size- and shape-dependent. It is therefore not surprising that the synthesis of nanomaterials of different shapes is actively pursued with the long-range objective of potential applications in promising fields. Materials with different dimensions such as (a) one-dimensional (1D) nanorods, nanowires, nanobelts, and nanotubes, (b) two-dimensional (2D) nanoplates, nanodisks, and nanofilms, and (c) three-dimensional (3D) nanocubes, have been prepared and reported on [1–4]. Especially, one-dimensional (1D) nanostructures such as carbon nanotubes have already been employed in the development of nanodevices [5]. Among the different categories of nanomaterials, rare earth based metal vanadates (RVO_4) have significant and insatiable interest in different fields.

Nanostructured rare earth orthovanadates, RVO_4 (R = La, Ce. Nd, Gd, Eu, Sm) have been widely studied in recent years due to their important properties. They have been used in catalysis [6], optical polarizers [7], gas sensors [8], lithium intercalated electrode [9], laser host materials [10], solar cells [11], thin film phosphors [12], and unusual magnetic materials [13]. Generally, the RVO_4 structure has two polymorphs, a monoclinic (*m*-) monazite-type and a tetragonal (*t*-) zircon-type [14]. The phase of the individual RVO_4 is dependent upon the ionic radii of rare earth elements. Because of the higher coordination number, the larger rare earth elements prefer to crystallize in the monazite phase type, as compared to the zircon type. However, $CeVO_4$ is placed in between the boundary of the monazite and zircon types. Here the deciding factors are synthetic conditions and pressure. Therefore, considering the importance of these novel materials many authors have reported on the synthesis of RVO_4 nanostructures using various synthetic methods based on wet chemical and dry processes. Using citrate method, RVO_4 (R = Y, La, Ce, Nd, Sm and Eu) particles were prepared and their catalytic properties have also been studied by oxidative dehydrogenation of propane [15]. A hydrothermal method has been reported for the synthesis of single crystalline tetragonal RVO_4 (R = La, Nd, Sm, Eu, Dy) nanorods [16]. Structural [17, 18] investigations of RVO_4 (R = Sm, Eu, Gd and Dy) and the photocatalytic activity [19] of RVO_4 (R = Ce, Pr, Nd) nanoparticles for the degradation of methylene blue have also been reported. Recently, Liu and Li reported on the preparation of colloidal RVO_4 (R = lanthanides) nanocrystals by an oleic acid-assisted hydrothermal method [20]. $LaVO_4$ nanocrystals [21], nanorods [14] and $CeVO_4$ nanocrystals [22] have also been prepared by the hydrothermal method. Wu et al. reported on the synthesis of $NdVO_4$ nanorods by a two-step strategy [23]. Even though, the hydrothermal method is a versatile technique to prepare the different morphological products it has some drawbacks; (i) the reaction kinetics is very slow at any given temperature [24] and (ii) it consumes prolonged time to complete the reaction for the specific morphology. Therefore, any simple method for the synthesis of 1D material will be a welcome addition.

In this regard, sonochemical method appears to be a versatile technique for the synthesis of nanoparticles of different morphologies such as nanorods [25], core-

shell nanorods [26], nanospindles [27], dendrites [28], etc. This is probably due to the ultrasound effect which leads to chemical changes through the cavitation phenomenon that involve the formation, growth, and collapse of the bubbles in liquids. During the sonication process, very high temperature (>5,000 K), pressure (1,800 atm) and cooling rates ($>10^8$ K/s) can be achieved upon the collapse of the bubbles, and this collapse probably leads to the production of desired nanostructures [29]. The sonochemical method is a simple process that doesn't entail a very complicated experimental setup and is eco-friendly. The reaction conditions are easily tunable, which enables the formation of nanomaterials of uniform size and shape by changing reaction parameters such as power, sonication time and solvents. Therefore, we have attempted to synthesize rare earth orthovanadate (RVO_4; R = La, Ce, Nd, Sm, Eu and Gd) nanoparticles/nanorods/nanospindles by the sonochemical method. To the best of our knowledge no such work has yet been reported on the synthesis of rare earth orthovanadates by a sonochemical method, except for a single report on $CeVO_4$ [30]. This is also the first report that presents the structural, optical, photocatalytic and electrocatalytic properties of RVO_4 (R = La, Ce, Nd, Sm, Eu and Gd) nanoparticles/nanorods/nanocrystals/nanospindles.

Experimental

All lanthanide precursors (0.01 M) and NH_4VO_3 (0.01 M) with >99.9% purity were purchased from Aldrich Co. and used as received without further purification. Polyethylene glycol (PEG-900) and amphiphilic triblock copolymer Pluronic P123 were used as structure-directing agents. The various lanthanide salts used for the synthesis of RVO_4 (R = La, Ce, Nd, Sm, Eu and Gd) are lanthanum acetate, cerium chloride, neodymium chloride, samarium nitrate, europium acetate and gadolinium chloride, respectively.

In a typical synthesis, 3.1605 g of La $(Ac)_3$ and 1.1691 g of NH_4VO_3 were dissolved in 90 mL of distilled water in a specially designed round-bottom sonication flask. 10 mL of PEG-900 was added to the above solution. The sonication flask was fixed in a water bath at room temperature (20–25 °C), and the system was irradiated in air by a high-intensity ultrasonic horn (Ti-horn, 20 kHz, 100 W/cm^2 at 70% efficiency) for 30 min. During sonication, 0.8 g of NaOH was added to the above mixture and sonication continued for a further 2½ h. The resultant product was collected, centrifuged at 9,000 rpm, washed several times using ethanol and distilled water, and then dried overnight under vacuum. To increase the crystallinity of the materials, the powders were further calcined at 500 °C for 5 h.

The X-ray diffraction patterns of the rare earth vanadates were measured with a Bruker AXS D* Advance Powder X-ray diffractometer (using Cu Kα = 1.5418 Å radiation). The particle morphology and structure were studied by transmission electron microscopy on a JEOL-JEM 100 SX TEM microscope, working at an 80 kV accelerating voltage. TGA of the as-synthesized samples were carried out under a stream of air at a heating rate of 10 °C min^{-1} from 25 °C to 850 °C using a Mettler Toledo TGA/STDA 851. Fourier transform infrared spectra (FTIR) were

recorded with a Coulter (Nicolet Impact-410) infrared spectrometer on KBr pellets in the region of 400–4,000 cm^{-1} with a 4 cm^{-1} resolution under ambient conditions. Raman spectra of all the RVO_4 were recorded on a Jobin Yvon Horiba Raman system. The 632.8-nm line of an He–Ne laser was used as the excitation source (40% power) focused to a 1–2 μm spot size. The diffuse reflectance UV–vis (DRUV) spectra were recorded for the powder samples on a Perkin–Elmer UV–visible spectrophotometer.

Photocatalytic studies with UV light were performed in a multilamp photoreactor fitted with eight 8 W mercury UV lamps of 365 nm wavelength (Sankyo Denki, Japan) and a highly polished anodized aluminum reflector; the sample was placed at the center of the photoreactor. Four cooling fans mounted at the bottom of the reactor dissipated the generated heat. The reaction vessel was a borosilicate glass tube with a 15-mm inner diameter. Photodegradation was also carried out in a micro photoreactor fitted with a 6 W 254 nm low-pressure mercury lamp and a 6 W 365 nm mercury lamp. Quartz and borosilicate glass tubes were used for 254 and 365 nm lamps, respectively. The light intensity was determined by ferrioxalate actinometry.

Fresh solutions of methylene blue of required concentrations were prepared in deionized distilled water. The volume of the reaction solution was always maintained as 25 mL in the multilamp photoreactor and 10 mL in the microreactor. Air was bubbled through the reaction solution. It effectively stirred the solution and kept the suspended catalyst under constant motion. After illumination, the catalyst was removed by centrifugation and the undegraded dye was estimated spectrophotometrically at 662.5 nm using a UV-1650 Shimadzu spectrophotometer. The dissolved oxygen was measured using an Elico dissolved oxygen analyzer, PE 135. Pre-sonication was carried out using a Toshcon SW 2 ultrasonic bath (37 ± 3 kHz, 150 W).

For the hydrogen evolution studies the electrode was prepared as detailed elsewhere [31]. Active materials (0.05 g) of the RE orthovanadate were dispersed in 0.25 mL of ethanol and 25 μL of 5 wt% Nafion. The dispersion was ultrasonicated for 30 min; 100 μL of the suspension was then coated on the titanium sheet (1 cm × 1 cm) and the solvent was slowly evaporated. Nafion (25 μL of 5 wt%, Aldrich) was again added on the coating and slowly evaporated. A Pt foil and Ag/AgCl/3 M NaCl were used as the counter and reference electrodes, respectively. The electrochemical studies were carried out using Princeton Applied Research (PAR) voltammetry. All the electrolyte solutions were deaerated with argon prior to the electrochemical measurements.

Results and Discussion

The thermograms of as-prepared RVO_4 nanoparticles/nanorods have been measured with a heating rate of 10 °C/min in static air from room temperature to 850 °C and given in supplementary data (Fig. S1). It shows that a single weight loss is obtained for all the samples, except for $LaVO_4$, between room temperature and ~500 °C. The observed percentages of weight loss are 13%, 5.7%, 8.7%, 9.6%, 9.9% and 10%

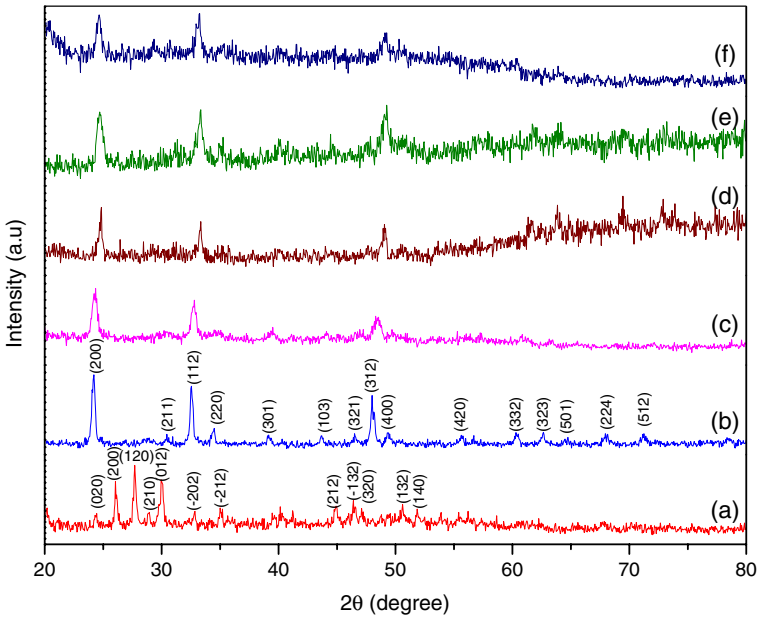

Fig. 1 XRD patterns of **a** $LaVO_4$, **b** $CeVO_4$, **c** $NdVO_4$, **d** $SmVO_4$, **e** $EuVO_4$ and **f** $GdVO_4$ nanostructures using PEG as the surfactant

for the as-prepared $LaVO_4$, $CeVO_4$, $EuVO_4$, $GdVO_4$, $NdVO_4$ and $SmVO_4$, respectively. This may be due to the loss of absorbed water or other residues of organic impurities like PEG. Above ~500 °C, no significant weight loss is observed for all the samples.

The crystallinity and phase purity of the synthesized rare earth orthovanadates were characterized by powder XRD patterns. Figure 1 presents the XRD patterns of the 500 °C calcined rare earth orthovanadates prepared by a sonochemical method using PEG as the surfactant. The patterns in Fig. 1a show sharp and well-defined peaks leading to the inference that following calcination, $LaVO_4$ is comprised of nanocrystalline material. The diffraction peaks are carefully indexed and assigned to the lattice planes of (020), (200), (120), (210), (012), (−202), (−212) and (212) for the corresponding 2θ values of 24.41, 26.14, 27.74, 28.91, 30.08, 32.82, 35.12 and 44.92, respectively. The observed pattern indicates that the prepared $LaVO_4$ material has a monoclinic structure with a space group of P21/n (14), corresponding to the JCPDS standard of 01-070-0216. Similarly, the rest of the vanadates, $CeVO_4$, $EuVO_4$, $GdVO_4$, $NdVO_4$ and $SmVO_4$, are indexed to the planes of (200), (211), (112), (220), (301), (103), (321), (312), (400), (420), (332), (323), (501), (224) and (512) for the predominant peaks. These data indicate the tetragonal structure of the materials with the space group of I41/amd (141) correlated to the JCPDS standards (JCPDS card numbers: 01-084-1457, 01-072-0859, 01-072-0279, 01-086-0995, 01-07-0277 for $CeVO_4$, $EuVO_4$, $GdVO_4$, $NdVO_4$ and $SmVO_4$, respectively). The calculated lattice constant values of $CeVO_4$: $a = 7.3574$ Å, $c = 6.4668$ Å; $NdVO_4$: $a = 7.3391$ Å, $c = 6.4241$ A°; $SmVO_4$: $a = 7.1780$ Å, $c = 6.3194$ Å; $EuVO_4$:

$a = 7.2132$ Å, $c = 6.3075$ Å; and $GdVO_4$: $a = 7.2132$ Å, $c = 6.3546$ Å confirmed the tetragonal structure of the materials.

The RVO_4 nanomaterials are further characterized by Raman spectroscopy. The Raman spectra of the RVO_4 (prepared by PEG as the surfactant) were measured in the range of 100–1,100 cm^{-1} and given in supplementary data (Fig. S2). The observed Raman peaks around 260, 380, 483, 810, 820 and 880 cm^{-1} confirm the existence of the vanadate ions [32, 33]. The observed prominent Raman peak values of $LaVO_4$, $CeVO_4$, $NdVO_4$, $SmVO_4$, $EuVO_4$ and $GdVO_4$ are 858.8, 861, 872, 879, 878, and 883 cm^{-1}, respectively, and they correspond to the symmetric stretching mode of the metal–oxygen bonds (–O–V–O–). It illustrates that the wave number values increase with the decrease in the ionic radii of the rare earth ions. This band shift is due to the lattice contraction of the vanadate structure, which leads to an increase in the bond strength [34]. It can be seen that the Raman spectra of $LaVO_4$ and $SmVO_4$ contain a larger number of peaks, as compared to the other vanadates which indicates the formation of some secondary phases in addition to the RVO_4. However, the presence of secondary phases is not revealed in the XRD patterns, either due to the low amount of these impurities or to their amorphous nature. The peaks around 146, 194, 285 (most intense), 305, 406, 485, 528, 704 and 996 cm^{-1} show the formation of V_2O_5 [35].

The FTIR spectra were recorded in the region of 400–4,000 cm^{-1} for the RVO_4 nanoparticles prepared using PEG as the surfactant and given in the supplementary data (Fig. S3). It can be seen that all the vanadates show a sharp and broad band around 452 cm^{-1} and 790 cm^{-1}, respectively, which are due to the stretching vibration of ν_s (VO_4) [15], and V–O [19], respectively. Another small band is observed for all the samples at 1,630 cm^{-1} corresponding to the bending vibration of H_2O molecules [36]. Among the vanadates, $LaVO_4$ shows some other bands around 618 and 1,023 cm^{-1} attributed to the vibrations of ν_{AS} (V–O–V) and δ (V=O), respectively. The bands at 1,023 cm^{-1} in $LaVO_4$ and 1,033 cm^{-1} in $SmVO_4$ are evidence of the presence of V_2O_5 in the samples [15]. No vibrational bands attributed to the PEG vibrational bands are detected in the IR spectra, indicating the complete removal of the surfactant.

UV–Vis spectra were recorded to characterize the optical properties of RVO_4 nanoparticles and are shown in Fig. 2. The powders are in fact dispersed on a carbon (tape)-coated ITO glass plate, after which the ITO slide acted as the substrate. It can be seen that strong absorption peaks at 257, 264, 267, 265, 266 and 263 nm are observed for $LaVO_4$, $CeVO_4$, $NdVO_4$, $SmVO_4$, $EuVO_4$, and $GdVO_4$, respectively. These prominent peaks are attributed to the UV absorption of the VO_4^{3-} of rare earth vanadates. In addition to this adsorption peak, the $NdVO_4$ shows some more peaks at 593 and 753 nm, which are attributed to the Nd^{3+} transition from $^4I_{9/2}$ to $^4G_{5/2}$ and $^4F_{7/2}$, respectively. This is in accordance with the observations of Wu et al. [23].

Figure 3 shows the TEM images of rare earth vanadates prepared by PEG as the surfactant. Though all the rare-earth vanadate particles are nanosized with different shapes, a wide distribution of sizes is obtained. While the $LaVO_4$ nanoparticles have a spherical shape with an average size in the range of 50–100 nm, the $CeVO_4$ particles are formed with both an oval shape (in the size range of 50–100 nm) and a spherical shape (10 nm in size). Surprisingly, $NdVO_4$ exhibits a nanowhisker

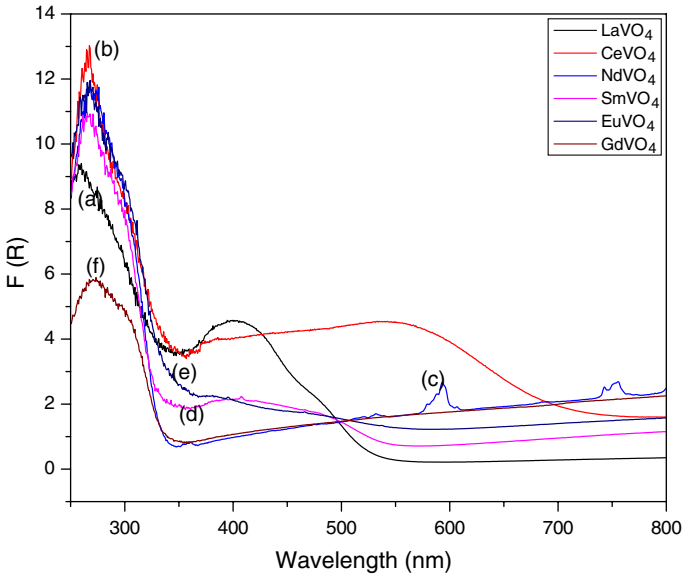

Fig. 2 UV-Vis spectra of **a** $LaVO_4$, **b** $CeVO_4$, **c** $NdVO_4$, **d** $SmVO_4$, **e** $EuVO_4$ and **f** $GdVO_4$ nanostructures using PEG as a surfactant

morphology with long tapered tips, with the largest width, ~10–25 nm, in the middle, and a length of 40–120 nm. In addition to the whiskers, some rod-shaped particles are also observed. The average length of the rods is 10–50 nm and that of the width is ~10 nm. The sonochemical method leads to the formation of spherical- and hexagonal-shaped particles of $SmVO_4$ with sizes ranging from 20–70 nm (Fig. 5d). Our method of synthesis of $EuVO_4$ yields an aggregation of particles comprised of bundles of small particles in the range of 15–50 nm. Spindle-type particles of $GdVO_4$ with various sizes were also observed.

To find the effect of surfactants on the morphological evolution of the vanadates, the same experiments have been carried out using P123 as the surfactant instead of PEG. Figure 4 depicts the TEM images of RVO_4 nanomaterials of different morphologies due to their molecular nature [37]. Interestingly, we obtained different morphologies from those obtained with PEG for the same products, which indicate that the surfactant plays a role in determining the size and the shape of the particles. $LaVO_4$ nanorods are formed with a size range of ~111–306 nm length and ~35–61 nm width. Similarly, $NdVO_4$ is fabricated as rod-like structures of 120–200 nm length and 20–30 nm width. Spindle-like structures are obtained for the $CeVO_4$ and $GdVO_4$ particles, but the size range is different. $GdVO_4$ has larger (~100 nm length and ~50 nm width) spindles. The $CeVO_4$ spindles are aggregated and form a flower-like structure. $SmVO_4$ also shows a flower-like morphology. On the other hand, $EuVO_4$ provides cubic-, hexagonal- and spherical- type crystals with sizes of less than 50 nm. These observed morphologies are entirely different from the materials prepared using PEG as the surfactant. When P123 is employed, with the exception of $EuVO_4$, we get 1 D materials for all the other RVO_4.

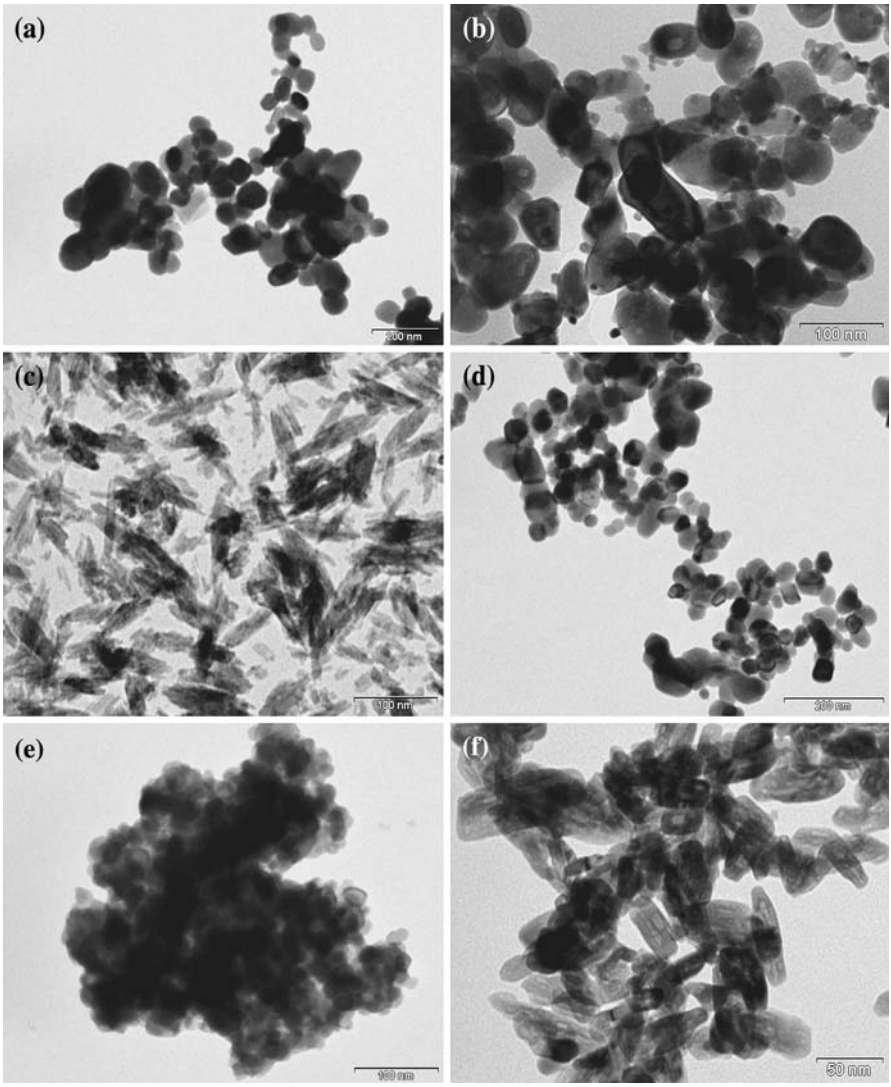

Fig. 3 TEM images of **a** $LaVO_4$, **b** $CeVO_4$, **c** $NdVO_4$, **d** $SmVO_4$, **e** $EuVO_4$ and **f** $GdVO_4$ nanostructures with PEG as the surfactant

To determine the role of sonication and the surfactant we carried out control experiments in the absence of sonication and the absence of surfactants in separate experiments and introduced in the supplementary data (Fig. S4a–c). In these control experiments we kept the other experimental conditions unchanged. Figure S4a provides the representative TEM image of $NdVO_4$ nanoparticles prepared in the absence of sonication and without a surfactant. The reaction was carried out at 70 °C for 3 h. It shows that the particles are aggregated and spherical-like with the size ranging between 10 and 30 nm. Figure S4b shows the TEM image

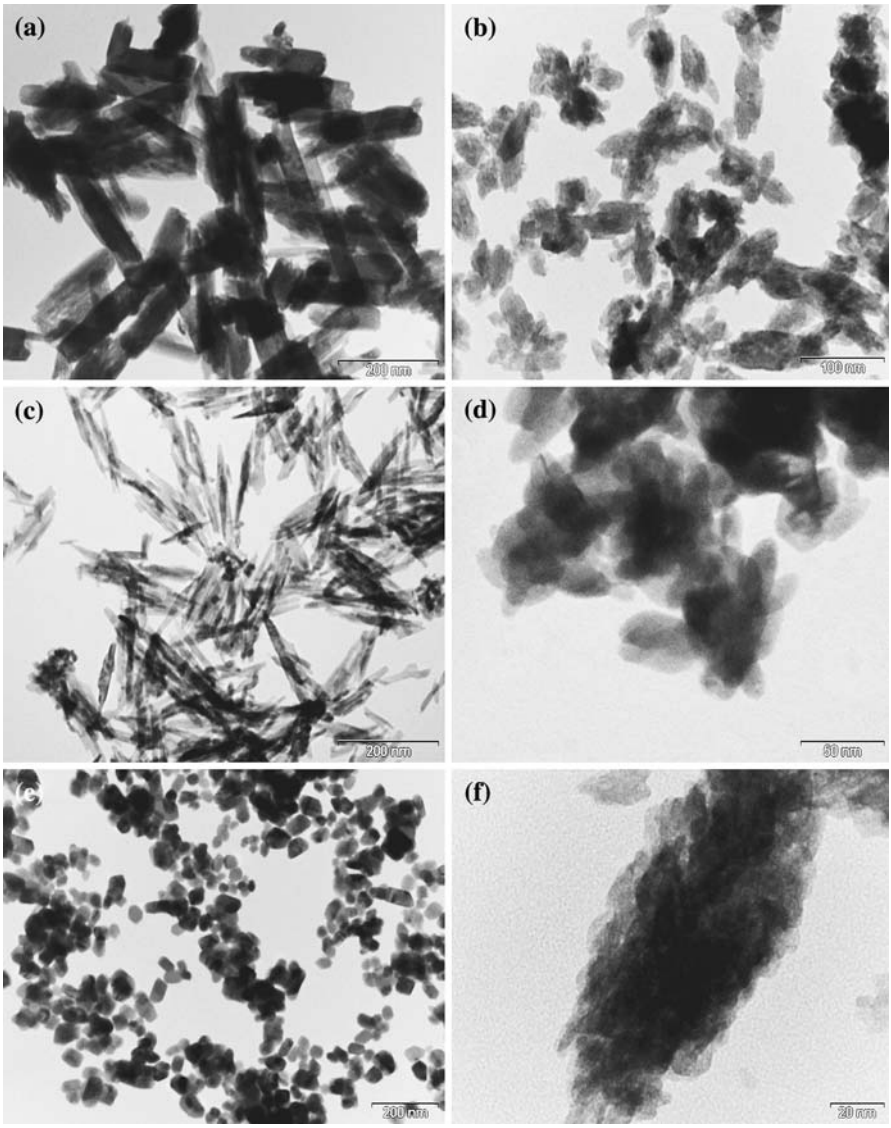

Fig. 4 TEM images of **a** $LaVO_4$, **b** $CeVO_4$, **c** $NdVO_4$, **d** $SmVO_4$, **e** $EuVO_4$ and **f** $GdVO_4$ nanostructures with P123 as the surfactant

of $NdVO_4$ nanoparticles prepared without sonication, but with a surfactant (P123). It shows that the particles are mainly aggregated and contain some spherical-shape particles with a size range of 20–30 nm. A small amount of rod-shaped particles are also observed ($\sim$20 nm length and $\sim$10 nm width). We can thus conclude that the P123 surfactant is responsible for the formation of rod-shaped particles. When applying both the surfactant and ultrasonics, we get the 100% rod-shaped particles with a size range of 120–200 nm length and 20–30 nm width (Fig. 4c). To find the

crystal growth mechanism of the rods, we carried out the same experiment at a lesser sonication time, 1 h. The TEM picture exhibits that the $NdVO_4$ (Fig. S4c) particles contain both the small rods (20–30 nm length and 10 nm width) with aggregated particles. The growth mechanism for the formation of 1D nanorods/nanospindles using the sonochemical method as a synthetic technique involves [38–40] nucleation formation under ultrasound irradiation, ultrasound-induced fusion of these primary nanoparticles accompanying the oriented growth to form rod-shaped particles, and the Ostwald ripening process. The individual nanorods are further aligned side by side to form spindle-shaped nanostructures. Our above results support the growth mechanism. Overall, it can be concluded that ultrasonics have played a vital role in preparing shape-dependent nanostructures.

The band gap values obtained from diffuse reflectance spectra are 3.1, 2.25, 2.15, 3.1, 3.26, 2.58 eV for $LaVO_4$, $CeVO_4$, $NdVO_4$, $SmVO_4$, $EuVO_4$, and $GdVO_4$, respectively, and these values are comparable to the band gap value of the well-known photocatalyst, TiO_2. Hence, the orthovanadates could act as photocatalysts under UV light. Degradation of methylene blue is used as the test reaction to examine the photocatalytic activities of the orthovanadates; photocatalysis by $CeVO_4$ has been studied in detail. We have employed $CeVO_4$ as the model compound because $LaVO_4$ dissolves in water (see Table 1). An aqueous solution of methylene blue in the presence of $CeVO_4$ was prepared and purged by air under illumination with the light of a wavelength of 365 nm. The methylene blue undergoes degradation**,** as seen from the absorbance spectra of the dye solution recorded at different time intervals after the recovery of the catalyst (Fig. 5). Experiments carried out in the dark reveal that the adsorption of the dye on the catalyst is insignificant compared to its degradation. The concentration-time profile (Fig. 6) shows that the degradation slackens after 30 min. Hence**,** the influence of operational parameters on the degradation was studied by measuring the degradation for 20 min; the measured degradation rates are reproducible to ±3%. The orthovanadate shows sustainable photocatalytic activity. Re-use of the catalyst yields identical degradation rates. The initial rate of degradation increases linearly with the dye-concentration, revealing first-order kinetics (Fig. 7a). This conforms to the Langmuir-Hinshelwood kinetic model under the condition that the

Table 1 The photocatalytic efficiencies of the vanadates, synthesised using PEG as the surfactant, to degrade methylene blue

Catalyst	Degradation, ppm h^{-1}
$LaVO_4$	14.1 (dissolves in water)
$CeVO_4$	11.4
$NdVO_4$	1.9
$SmVO_4$	8.6
$EuVO_4$	6.1
$GdVO_4$	6.1

[MB] = 10 ppm; catalyst-loading = 0.02 g; λ = 365 nm; photon flux = 25.2 μeinstein L^{-1} s^{-1}; pH = 7.3; airflow rate = 7.8 mL s^{-1}; $[O_2]_{dissolved}$ = 5.6 mg L^{-1}; volume of solution = 25 mL

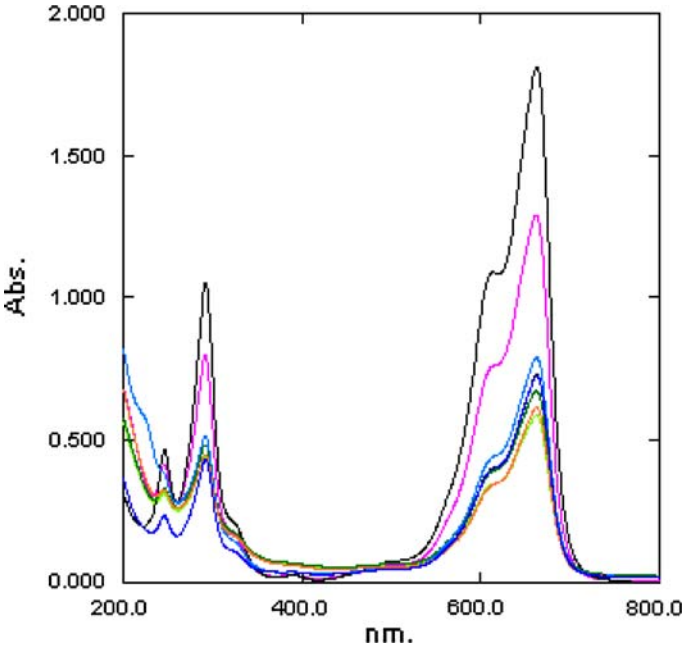

Fig. 5 Photodegradation of methylene blue with $CeVO_4$. The UV–Vis spectra of the illuminated dye solution recorded at 0, 15, 30, 45, 60, 75, 90 min (↓). $[MB]_0 = 10.0$ ppm, catalyst loading = 0.02 g, pH = 7.3, $\lambda = 365$ nm, $I = 25.2$ μeinstein L^{-1} s^{-1}, airflow rate = 7.8 mL s^{-1}, $[O_2]_{dissolved} = 5.6$ mg L^{-1}, MB solution = 25 mL

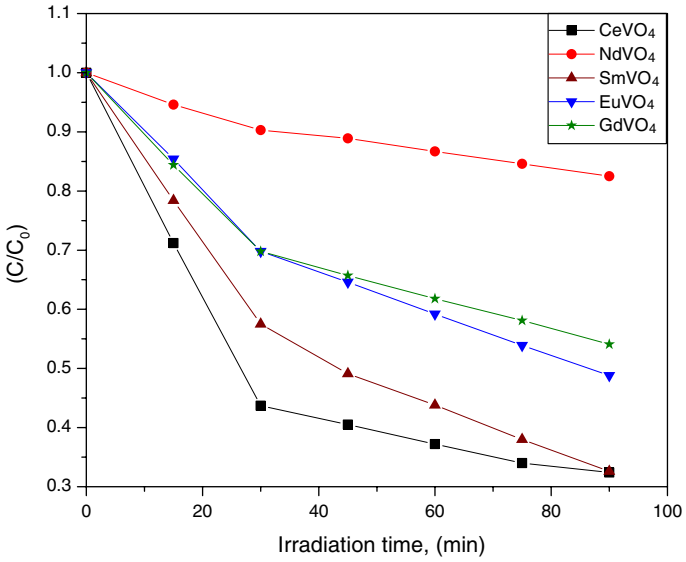

Fig. 6 Photodegradation on RVO_4 nanostructures. The concentration-time profile: Catalyst loading = 0.02 g, pH = 7.3, $\lambda = 365$ nm, $I = 25.2$ μeinstein L^{-1} s^{-1}, airflow rate = 7.8 mL s^{-1}, $[O_2]_{dissolved} = 5.6$ mg L^{-1}, MB solution = 25 mL

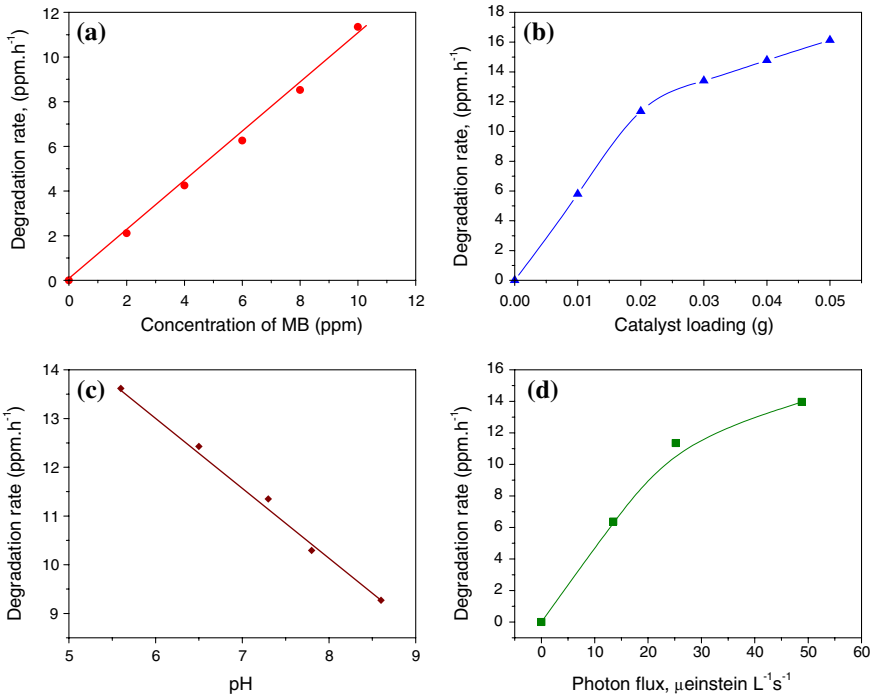

Fig. 7 **a** Linear dependence of degradation rate on [MB]. Catalyst loading = 0.02 g, pH = 7.3, λ = 365 nm, I = 25.2 μeinstein L^{-1} s^{-1}, airflow rate = 7.8 mL s^{-1}, $[O_2]_{dissolved}$ = 5.6 mg L^{-1}, MB solution = 25 mL. **b** Photodegradation as a function of $CeVO_4$ loading. $[MB]_0$ = 10.0 ppm, pH = 7.3, λ = 365 nm, I = 25.2 μeinstein L^{-1} s^{-1}, airflow rate = 7.8 mL s^{-1}, $[O_2]_{dissolved}$ = 5.6 mg L^{-1}, MB solution = 25 mL. **c** Variation of degradation with pH. $[MB]_0$ = 10.0 ppm, catalyst loading = 0.02 g, λ = 365 nm, I = 25.2 μeinstein L^{-1} s^{-1}, airflow rate = 7.8 mL s^{-1}, $[O_2]_{dissolved}$ = 5.6 mg L^{-1}, MB solution = 25 mL. **d** Photodegradation as a function of photon flux. $[MB]_0$ = 10.0 ppm, catalyst loading = 0.02 g, pH = 7.3, λ = 365 nm, airflow rate = 7.8 mL s^{-1}, $[O_2]_{dissolved}$ = 5.6 mg L^{-1}, MB solution = 25 mL

dye-adsorption on the illuminated catalyst surface is small (K [MB] << 1, where K is the adsorption coefficient of the dye on the illuminated catalyst). The degradation rate increases linearly at low loading of the catalyst, but not so at high loading due to a screening effect (Fig. 7b). At high catalyst loading, the surface area of the catalyst exposed to illumination is not commensurate with the weight of the catalyst used; the loaded catalyst is beyond the critical amount corresponding to the volume of the dye solution and the reaction vessel. Pre-sonication for 10 min at 37 ± 3 kHz and 150 W suppresses the photocatalysis to about 60% (conditions as in Fig. 8)**.** An increase in the pH of the medium slows down the degradation (Fig. 7c); the pH of the solution was controlled by the addition of an acid or an alkali. The photocatalysis lacks linear dependence on the photon flux, varied by using two, four or eight lamps (Fig. 7d); the angles sustained by the adjacent lamps at the sample were 180, 90 and 45°. Less than first power dependence of the surface-photocatalysis rate on light intensity at high photon flux is well known [41]. The illumination of the catalyst at a lower wavelength shows a moderately enhanced

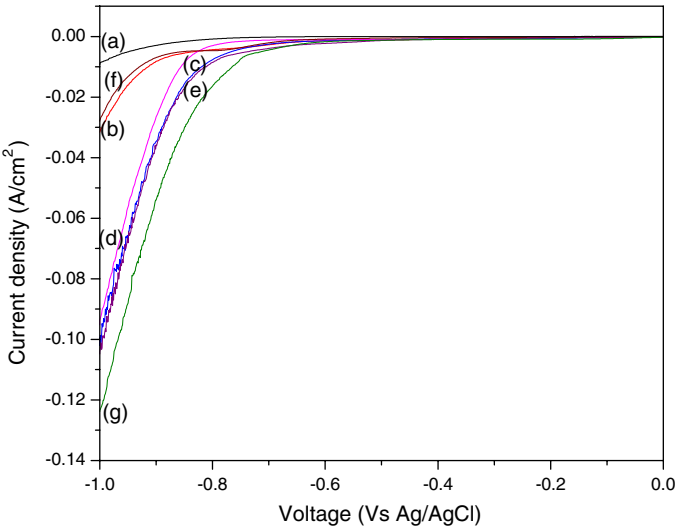

Fig. 8 Hydrogen evolution reaction of **a** Ti substrate, **b** $LaVO_4$, **c** $CeVO_4$, **d** $NdVO_4$, **e** $SmVO_4$, **f** $EuVO_4$ and **g** $GdVO_4$ nanostructures with PEG as the surfactant in 1 M H_2SO_4 at a scan rate of 1 mV/s

degradation; the degradation rates determined in a micro-reactor with the light of wavelengths 254 and 365 nm are 15.7 and 13.4 ppm h^{-1}, respectively (10 mL of 10 ppm methylene blue with 0.02 g catalyst at pH 7.3 with an airflow rate of 7.8 mL s^{-1} corresponding to 5.6 mg L^{-1} of dissolved oxygen and a photon flux of 5.22 and 18.1 μeinstein L^{-1} s^{-1}, respectively). Since the catalyst absorbs in the visible region, there is no large enhancement in the degradation on illumination at shorter wavelengths. The photocatalytic efficiencies of all the six lanthanum orthovanadates were examined at optimum conditions (see Table 1). $LaVO_4$ is the best photocatalyst, but it dissolves in water. The dissolution of $LaVO_4$ in water does not allow its re-use as a photocatalyst. $CeVO_4$ is therefore the most efficient in the heterogeneous photocatalytic reaction. $NdVO_4$ is less efficient for photodegrading methylene blue, and the other RE vanadates show comparable catalytic efficiencies to that of $CeVO_4$. The mechanism of photocatalysis is as follows. The band gap illumination of the semiconductor generates electron-hole pairs, electrons in the conduction band, and holes in the valence band [42]. A portion of these electron-hole pairs diffuses out to the surface of the crystal and participates in chemical reactions with electron donors and acceptors, leading to photocatalysis. As the recombination of the electron-hole pairs is very fast, the reactants must be adsorbed on the semiconductor for an effective photocatalysis [43]. While the hole oxidizes the organics [44] the electron is taken up by the adsorbed oxygen molecule, yielding a highly active superoxide radical, $O_2^{\bullet -}$. In an aqueous medium, $O_2^{\bullet -}$ in turn generates reactive species such as $HO^{\bullet}$, $HO_2^{\bullet}$ and H_2O_2, which also oxidize the dye. Water is adsorbed on the semiconductor, molecularly and dissociatively [45, 46]. Hole trapping by either the surface hydroxyl groups or adsorbed water molecules results in short-lived $HO^{\bullet}$ radicals, which are the primary oxidizing agents [47–50].

The electrocatalytic properties of the nanomaterials have been studied for hydrogen evolution owing to its environmental friendliness and high energy density. As hydrogen will be the future source of energy for replacing the existing energy systems, hydrogen evolution reaction (HER) is believed to be one of the most important reactions in water electrolysis. Figure 8 shows the linear sweep voltammogram of RVO_4 nanoparticles in the potential range of 0.0 to −1.0 V at a scan rate of 1 mV/s in a 1 M H_2SO_4 solution. It shows that the all the vanadates are active as electrocatalysts when compared to the bare Ti electrode. The observed onset potentials of $LaVO_4$, $CeVO_4$, $NdVO_4$, $SmVO_4$, $EuVO_4$, and $GdVO_4$ are −0.640 V, −0.51 V, −0.721 V, −0.452 V, −0.663 V and −0.551 V, respectively. The current values reached at −1 V are −31.6, −102, −95.2, −105, −28.0, and −124 mA/cm^2 for the $LaVO_4$, $CeVO_4$, $NdVO_4$, $SmVO_4$, $EuVO_4$, and $GdVO_4$, respectively. This current value is larger when compared to the bare Ti electrode value of −9 mA/cm^2 at −1 V. This shows that the materials have the ability to adsorb/intercalate more protons in the lattice structure [31]. In addition, surface composition, defect density, crystallographic orientation, and electronic surface structures are critical parameters for determining the electrocatalytic properties of the materials [51]. Among the examined systems $GdVO_4$ gives a higher current value, indicating that it is a good electrocatalyst. However, in the case of photocatalytic studies, $CeVO_4$ acts as a good catalyst for degrading the MB. For electrocatalytic properties, the electrochemical surface area (ESA) plays an important role in inducing the catalytic activity of the materials [52].

Conclusions

The synthesis of RVO_4 (R = La, Ce, Nd, Sm, Eu and Gd) nanoparticles/nanorods/nanospindles has been achieved by a sonochemical technique employing two different surfactants. The morphologies of the orthovanadates have been studied by electron microscopy. When the surfactant PEG was employed, nanorods of $NdVO_4$ and nanospindles of $GdVO_4$ were obtained. However, a PEG structure-directed method yielded nanoparticles of other orthovanadates. With the P123 surfactant, the sonochemical synthesis results in the formation of nanorods. These results indicate that in the sonochemical method the shapes of nanomaterials can be tuned. The photocatalytic and electrocatalytic properties of the RVO_4 materials have been investigated. Among the rare earth vanadates, $CeVO_4$ acts as the best photocatalyst for the degradation of methylene blue, and $GdVO_4$ acts as a good electrocatalytic material in terms of hydrogen evolution studies.

References

1. S. M. Lee, S. N. Cho, and J. Cheon (2003). *Adv. Mater.* **15**, 441.
2. M. J. Siegfried and K. S. Choi (2005). *Angew. Chem. Int. Ed.* **44**, 3218.
3. Z. T. Zhang, A. J. Rondinone, J. X. Ma, J. Shen, and S. Dai (2005). *Adv. Mater.* **17**, 1415.

4. C. R. Patra, G. Alexandra, S. Patra, D. S. Jacob, A. Gedanken, A. Landau, and Y. Gofer (2005). *New J. Chem.* **29**, 733.
5. K. Jensen, J. Weldon, H. Garcia, and A. Zettl (2007). *Nano Lett.* **7**, 3508.
6. C. T. Au and W. D. Zhang (1997). *J. Chem. Soc. Faraday Trans.* **93**, 1195.
7. F. Chen, X. Wang, S. Li, G. Fu, K. Wang, Q. Lu, D. Shen, R. Nie, and H. Ma (2003). *J. Appl. Phys.* **94**, 4708.
8. E. V. Tsipis, M. V. Patrakeev, V. V. Kharton, N. P. Vyshatko, and J. R. Frade (2002). *J. Mater. Chem.* **12**, 3738.
9. G. Picardi, F. Varsano, F. Decker, U. O. Krasovec, A. Surca, and B. Orel (1999). *Electrochim. Acta.* **44**, 3157.
10. R. A. Fields, M. Birnbaum, and C. L. Fincher (1987). *Appl. Phys. Lett.* **51**, 1885.
11. J. F. Liu, Q. H. Yao, and Y. D. Li (2006). *Appl. Phys. Lett.* **88**, 173119.
12. M. Yu, J. Lin, and S. B. Wang (2005). *Appl. Phys. A: Mater. Sci. Proc.* **80**, 353.
13. K. Gaur and H. B. Lal (1983). *J. Mater. Sci. Lett.* **2**, 744.
14. W. Fan, X. Song, Y. Bu, S. Sun, and X. Zhao (2006). *J. Phys. Chem. B* **110**, 23247.
15. C. T. Au, W. D. Zhang, and H. L. Wan (1996). *Catal. Lett.* **37**, 241.
16. W. Fan, W. Zhao, L. You, X. Song, W. Zhan, H. Yu, and S. Sun (2004). *J. Solid State Chem.* **177**, 4399.
17. D. F. Mullica, E. L. Sappenfield, M. M. Abraham, B. C. Chakoumakos, and L. A. Boatner (1996). *Inorg. Chim. Acta.* **248**, 85.
18. S. Mahapatra and A. Ramanan (2005). *J. Alloy. Compd.* **395**, 149.
19. S. Mahapatra, G. Madras, and G. Row (2007). *Ind. Eng. Chem. Res.* **46**, 1013.
20. J. Liu and Y. Li (2007). *J. Mater. Chem.* **17**, 1797.
21. N. Wang, Q. Zhang, and W. Chen (2007). *Cryst. Res. Technol.* **42**, 138.
22. F. Luo, C. J. Jia, W. Song, L. P. You, and C. H. Yan (2005). *Cryst. Growth Des.* **5**, 137.
23. X. Wu, Y. Tao, L. Dong, J. Zhu, and Z. Hu (2005). *J. Phys. Chem. B.* **109**, 11544.
24. S. Komarneni (2003). *Curr. Sci.* **85**, 1730.
25. L. H. Qiu, V. G. Pol, M. J. Calderon, and A. Gedanken (2005). *Ultrasonic Sonochem.* **12**, 243.
26. L. Zhu, X. Liu, Q. Li, J. Li, S. Zhang, J. Meng, and X. Cao (2006). *Nanotechnology* **17**, 4217.
27. J. Geng, J. J. Zhu, D. J. Lu, and H. Y. Chen (2006). *Inorg. Chem.* **45**, 8403.
28. J. Geng, Y. Lv, D. Lu, and J. J. Zhu (2006). *Nanotechnology* **17**, 2614.
29. V. G. Pol, R. Reisfeld, and A. Gedanken (2002). *Chem. Mater.* **14**, 3920.
30. L. Zhu, Q. Li, J. Li, X. Liu, J. Meng, and X. Cao (2007). *J. Nanoparticle Res.* **9**, 261.
31. R. Ganesan and A. Gedanken (2008). *Nanotechnology* **19**, 025702.
32. C. C. Santos, E. N. Silva, A. P. Ayala, I. Guedes, P. S. Pizani, C. K. Loong, and L. A. Boatner (2007). *J. Appl. Phys.* **101**, 053511.
33. I. Guedes, Y. Hirano, M. Grimsditch, N. Wkabayashi, C. K. Loong, and L. A. Boatner (2001). *J. Appl. Phys.* **90**, 1843.
34. N. Deligne, V. Gonze, D. Bayot, and M. Devillers (2008). *Eur. J. Inorg. Chem.* **6**, 896.
35. C. Julien, G. A. Nazri, and O. Bergstrom (1997). *Phys. Stat. Sol.* **201**, 319.
36. M. Gotić, S. Musić, M. Ivanda, M. Šoufek, and S. Popović (2005). *J. Mol. Struct.* **744–747**, 535.
37. P. Alexandridis and T. A. Hatton (1995). *Colloid Surf. Sci. A* **96**, 1.
38. J. Geng, D. Lu, J. J. Zhu, and H. Y. Chen (2006). *J. Phys. Chem. B* **110**, 13777.
39. C. J. Mao, H. C. Pan, X. C. Wu, J. J. Zhu, and H. Y. Chen (2006). *J. Phys. Chem. B* **110**, 14709.
40. L. Zhu, X. Liu, J. Meng, and X. Cao (2007). *Cryst. Growth Des.* **7**, 2505.
41. L. Vincze and T. J. Kemp (1995). *J. Photochem. Photobiol. A* **87**, 257.
42. M. R. Hoffmann, S. T. Martin, W. Choi, and D. W. Bahnemann (1995). *Chem. Rev.* **95**, 69.
43. T. L. Thompson and J. T. Yates Jr. (2006). *Chem. Rev.* **106**, 4428.
44. Y. Tamaki, A. Furube, M. Murai, K. Hara, R. Kotoh, and M. Tachiya (2006). *J. Am. Chem. Soc.* **128**, 416.
45. R. Osgood (2006). *Chem. Rev.* **106**, 4379.
46. J. Zhao, B. Li, K. Onda, M. Feng, and H. Petek (2006). *Chem. Rev.* **106**, 4402.
47. Y. Shiraishi, N. Saito, and T. Hirai (2005). *J. Am. Chem. Soc.* **127**, 12820.
48. J. Peller, O. Wiest, and P. V. Kamat (2004). *J. Phys. Chem. A* **108**, 10925.
49. Y. Du and J. Rabani (2003). *J. Phys. Chem. B* **107**, 11970.
50. L. Sun and J. R. Bolton (1996). *J. Phys. Chem.* **100**, 4127.
51. L. A. Kibler (2006). *Chem. Phys. Chem.* **7**, 985.
52. R. Ganesan, D. J. Ham, and J. S. Lee (2007). *Electrochem. Commun.* **9**, 2576.